ADVANCED FUNCTIONAL MATERIALS
www.afm-journal.de

Peptide-Guided Self-Assembly: Fabrication of Tailored Spiral-Like Nanostructures for Precise Inorganic Templating

Alberto Alvarez-Fernandez, Nisha Pawar, Pablo Sanchez-Puga, Nathan. R. Zaccai, and Armando Maestro**

Self-assembling peptides (SAPs) are versatile building blocks in the creation of hierarchical nanostructures. Although SAPs promise precise control over assembled morphology and dimensions, experimental validation is still crucial. In this sense, recent efforts have focused on nanospiral structures, which mimic natural architectures and hold potential for biomedical and nanotechnological applications. Here, it is demonstrated that SARS-CoV-2 fusion peptides are able to form specific spiral-like structures using interfacial assembly as a fabrication methodology, along with fine-tuning of the spiral ensembles through an imposed interfacial flow due to the uniaxial compression in a Langmuir–Blodgett trough. Molecular characterization by atomic force microscopy, neutron reflectometry, interfacial shear rheology, and infrared spectroscopy, highlighted how variations in fusion peptide sequences influence assembly, highlighting the importance of molecular design. These spiral structures are subsequently modified to serve as templates for metallic replicas, expanding the potential of peptide-guided self-assembly in fabricating tailored nanostructured surfaces with sub-10 nm dimensions over cm^2 areas.

1. Introduction

Spiral-like nanostructures have garnered significant attention due to their unique properties, particularly those associated with their chirality. Thus, the preparation of such spirals using metallic species like gold or silver is crucial for tailoring their surface plasmon resonance responses, leading to unique optical, electronic, and catalytic properties.[1,2] However, most research to date has focused on theoretical and computational simulations, primarily due to fabrication challenges and the limited availability of techniques capable of producing these complex structures.[1,3] While methods such as electron-beam or colloidal lithography have been explored,[1,2] they do not yet offer precise control over parameters such as curvature degree and interspacing of the resulting spiral structures, limiting their applicability.

In pursuit of new fabrication methodologies for the formation and tuning of spiral nanostructures, interfacial assembly has recently emerged as a promising alternative. It is well established that fluid interfaces can serve as versatile platforms for promoting the spontaneous self-assembly of colloidal systems, driven by the reduction in interfacial energy.[4] External forces, such as interfacial flow induced by uniaxial compression in a Langmuir–Blodgett (LB) trough, allow for precise control over the organization of colloidal objects.[5] As a result, a wide variety of interfacial structures can be achieved, ranging from liquid-like arrangements to solid-like structures (such as gels or colloidal glasses), with diverse morphologies.[6]

Following this methodology, Huang et al demonstrated the formation of well-defined spiral-shaped nanostructures from barbituric acid derivatives through interfacial assembly, driven by compression in a LB trough.[7,8] The generated compressive forces induced hydrogen bonding between the blocks, facilitating their directional assembly and leading to the formation of chiral spirals at the fluid interphase. Zhang et al. further expanded on this concept by employing anthracene derivatives, where π–π staking interactions between the anthracene groups promoted the formation of spiral-like structures.[9] Interestingly, they observed a morphological transition from coiled structures to straight nanoribbons with increased pressure, which introduced switching photocurrent behavior. Despite these promising developments,

A. Alvarez-Fernandez, N. Pawar, A. Maestro
Centro de Física de Materiales (CFM) (CSIC–UPV/EHU)
Materials Physics Center (MPC)
Paseo Manuel de Lardizabal 5, Donostia-San Sebastián 20018, Spain
E-mail: alberto.alvarez@ehu.eus; armando.maestro@ehu.eus

P. Sanchez-Puga
Large Scale Structures group
Institut Laue-Langevin
71 Avenue des Martyrs, Grenoble 38042 Cedex 9, France

N. R. Zaccai
Cambridge Institute for Medical Research
University of Cambridge
Cambridge CB22 7QQ, UK

A. Maestro
IKERBASQUE-Basque Foundation for Science
Plaza Euskadi 5, Bilbao 48009, Spain

The ORCID identification number(s) for the author(s) of this article can be found under https://doi.org/10.1002/adfm.202411061

DOI: 10.1002/adfm.202411061

several challenges persist, limiting the practical applications of these fabrication methodologies. These include the necessity of incorporating functional or responsive groups into the building blocks to promote their assembly into spiral structures, limited structural control over the resulting nanostructures, and difficulties in transferring these patterns into metallic structures.

In the search for new building blocks for fabricating highly controllable spiral-like structures, self-assembling peptides (SAPs) offer a promising alternative. SAPs have gained significant interest as innovative building blocks for creating tailored and precisely controllable nanostructures, including nanospheres, nanotubes, nanosheets, and hydrogels.[10–13] These materials frequently present the unique advantage of generating hierarchical 2D or 3D architectures, which are challenging to achieve through conventional bottom-up approaches like colloidal or block copolymer self-assembly. Generally, SAPs consist of short peptide sequences capable of spontaneously assembling and organizing into well-ordered nanostructures,[11] via non-covalent interactions, including electrostatic forces, hydrogen bonding, and hydrophobic/hydrophilic interactions.[14] In this context, Wen and coworkers have recently shown the possibility of SAPs for forming spiral structures via the incorporation of photo-responsive functional groups, which induce structural bending upon light exposure.[15] However, a fabrication methodology that enables the generation of spiral assemblies without relying on complex molecular design or complicated fabrication techniques is still needed.

In response, this work introduces interfacial assembly and uniaxial compression forces as effective methodologies for fabricating highly tunable spiral-like structures using peptides derived from the SARS-CoV-2 virus as building blocks. From a biological perspective, the viral Spike protein is cleaved by proteolysis (at residue 816), which frees the protein's fusion domain to initiate membrane fusion. Putative Spike fusion peptides used in this study include FP1 (SARS-CoV-2 816–837), and FP2 (835–856), which are characterized by their short-length, and high hydrophobicity. To form the assembled nanofibril structures, these two fusion peptides were deposited at the air–water interface using an LB trough. Structural information about the resultant spiral-like nanostructures formed upon compression was obtained using atomic force microscopy (AFM) and Fourier-transform infrared spectroscopy (FTIR). Additionally, neutron reflectometry (NR) and shear rheology measurements were employed to track the assembly process. The resulting spiral-like structures were subsequently utilized as templates for the fabrication of metallic replicas, paving the way for their potential applications in optical and nanofabrication technologies.

2. Results and Discussion

2.1. Methodology to Study Nanostructure Formation

The direct self-assembly of two distinct peptides derived from the SARS-CoV-2 Spike fusion core, designated as FP1 and FP2, was investigated.[16] The primary objective was to explore how interfacial assembly could be achieved with fluid interfaces acting as templates. Through uniaxial compression in the LB trough, it was possible to finely tune the morphology, orientation, and packing density of the various self-organized structures formed by each peptide at the air/water interface.

Spiral-like nanostructures could be formed by interfacial assembly (**Figure 1**). Briefly, peptide solutions in dimethyl sulphoxide (DMSO) were prepared (Figure 1A), prior to their deposition at the air–water interface using a LB trough (Figure 1B). The Langmuir trough barriers then exerted lateral, unidirectional compression at a constant speed until reaching surface pressures of 10, 20 or 30 mN m^{-1}. The resultant peptide films were transferred onto a mica solid substrate and analyzed by peak-force tapping AFM (Figure 1C). The obtained nanostructures were subsequently used as templates for fabricating metallic replicas (Figure 1D).

2.2. Nanofibril Formation Resulting in Spiral-Like Nanostructures

AFM micrographs of the peptide LB films transferred onto freshly cleaved mica substrates at surface pressures of 2 mN m^{-1} (without compression) and 20 mN m^{-1} (compression ratio of 2.5) respectively are presented in **Figure 2**B–E. The adsorption of both FP1 and FP2 peptides onto the mica surfaces could be confirmed and can be attributed to electrostatic interactions between the peptides' charged residues and the SiO^- groups on the mica surface.[17]

The AFM analysis indicated that the absence of compression resulted in random peptide aggregates on the mica surface. An increase of $\prod$ to 20 mN m^{-1} promotes the formation of elongated and flexible nanofibrils for both FP1 and FP2. A profile analysis revealed that the filaments predominantly exhibited a nanofibril structure. The observed distributions of fibril heights 2.0 ± 0.2 nm and 1.8 ± 0.1 nm for FP1 and FP2, respectively (see AFM topographical profiles in Figure S1, Supporting Information) are consistent with a peptide monolayer whose backbones are aligned parallel to the mica substrate. This conformation is further supported by the molecular size calculations of both peptides, assuming a β-strand structure, as will be discussed later. Figure S2 (Supporting Information) illustrates the 3D representation of the molecular structures of both FP1 and FP2. It shows dimensions of ≈7.4 nm in length and 1.3 nm in height, which align with the fiber dimensions observed on the mica surfaces. Moreover, previous theoretical and experimental observations have demonstrated that the peptides align parallel to the surface even when deposited onto hydrophilic surfaces.[17,18] Given that in this work the fiber formation occurs at the air–water interface, this parallel orientation is even more favorable (Figure 2F,G).

2.3. Nanofibrils Consist Predominantly of β-Strands

The formation of such structures is directly influenced by peptides´ secondary structure. Indeed, previous studies demonstrated the formation of a β-sheet structure enhances the capability of the peptides to generate layers and fibers when interfacing with solid surfaces.[19,20] To confirm the presence of

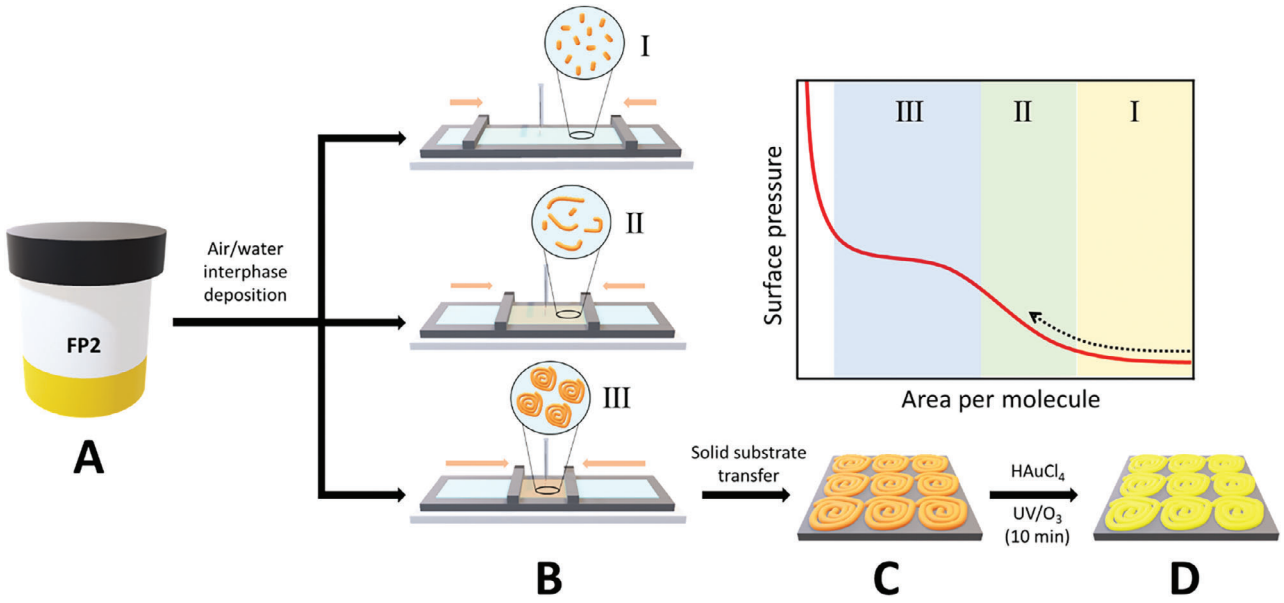

Figure 1. Schematic summary of the experimental approach. A) Preparation of the peptide solution into DMF. B) Deposition at the air–water interfase and compression using a LB set-up. C) Transfer to mica substrate. D) Selective impregnation with metallic salt and peptide removal with UV/O_3.

peptide secondary structure within the observed fibers, we employed Laser Direct Infrared (LDIR) in reflection mode, focusing on the amide I band (1600–1700 cm^{-1}), to analyze the self-assembled surfaces. The Amide I band, primarily associated with the stretching vibration of the carbonyl group (CO), is widely recognized for its sensitivity to different types of protein secondary structures.[21] Figure 2H shows the LDIR spectra of the surfaces studied. Secondary structure prediction by JPRED identified the putative presence of α-helical and β-strands elements in both peptides (see Figure S3, Supporting Information).[22]

The application of compression forces on FP2 peptides led to the emergence of a prominent absorption band at 1623 cm^{-1}, indicative of the peptides adopting β-sheet conformations. Remarkably, as expected for anti-parallel (AP) β sheets, the amide I LDIR spectrum in Figure 2H shows a relatively strong perpendicular mode $\nu_{\perp}$ at ≈1620 cm^{-1} and a weaker intensity parallel mode at $\nu_{\parallel}$ ≈1680 cm^{-1}.[23]

In the case of uniaxial strain applied to self-assembled FP1 peptides, a strong absorption band in the region 1620–1650 cm^{-1} is present, which is compatible with the existence of the expected β-sheets, but also of α-helices and random coils, as the latter typically appear at ≈1640–1650 cm^{-1}.

In view of this analysis, the AFM data suggests that peptidepeptides' β-strands self-assemble into ladders that are oriented perpendicular to the long axis of the filament and parallel to the surface (Figure 2F,G). As previously introduced, the height distribution of the fibril can be rationalized as the stacking of several β-strands given that a single β-strand usually contributes ≈3.5 A per residue in height.[24] Besides, the width distribution suggests that the fibril consists of several β-sheets arranged side-by-side. Each β-sheet is likely composed of several β-strands aligned in an antiparallel configuration. Such level of organization is characteristic of many amyloid fibrils and similar protein assemblies that form filaments in biological systems.[11,25]

Consequently, the nanofibrils predominantly consist of AP β-sheets lying flat on the air/water interface. This secondary structure and conformation was previously observed for HIV fusion peptides.[26] However important differences in peptide secondary structure are also detected. In the case of FP1, the contribution of the AP β-sheets is smaller than in FP2, with higher intensity of the random-coil and α-helix structure (Figure 2I). The higher contribution of the latter, ompared to FP2, suggests more rigid fibers, due to the increased rigidity of the α-helix conformation relative to other secondary structures.

2.4. Difference in Morphology Between FP1 and FP2 Spiral-Like Nanostructures

Differences in rigidity can be clearly detected in the AFM micrographs presented in Figure 2D,E. Thus, fibers derived from FP1 exhibit considerable length with minimal curvature, while those derived from FP2 display pronounced curvature, folding upon themselves to form intricately organized nanospirals. The curvature degree of the fibers has been quantitatively analyzed in Figure S4 (Supporting Information). Thus, the curvature angle distribution (θ) for FP1-based fibers is measured at 172 ± 4°, while FP2 fibers exhibit a θ of 164 ± 5° under the same compression forces.

We model FP1 and FP2 peptide fibrils as worm-like chains,[27] and measure the persistence length (L_p) based on the relationship between the fibrils' contour length, and their end-to-end distance (Figure S5, Supporting Information).[28] FP1 fibrils have a characteristic L_p of 3.2 ± 0.2 µm, while FP2 shows a decrease in L_p to 0.12 ± 0.03 µm. These values are consisting with previous similar fibrillar peptides.[29] As expected, FP1 fibers, with a larger L_p, exhibit greater stiffness and less curvature showing and almost rigid rod conformation compared to FP2 fibers, which have

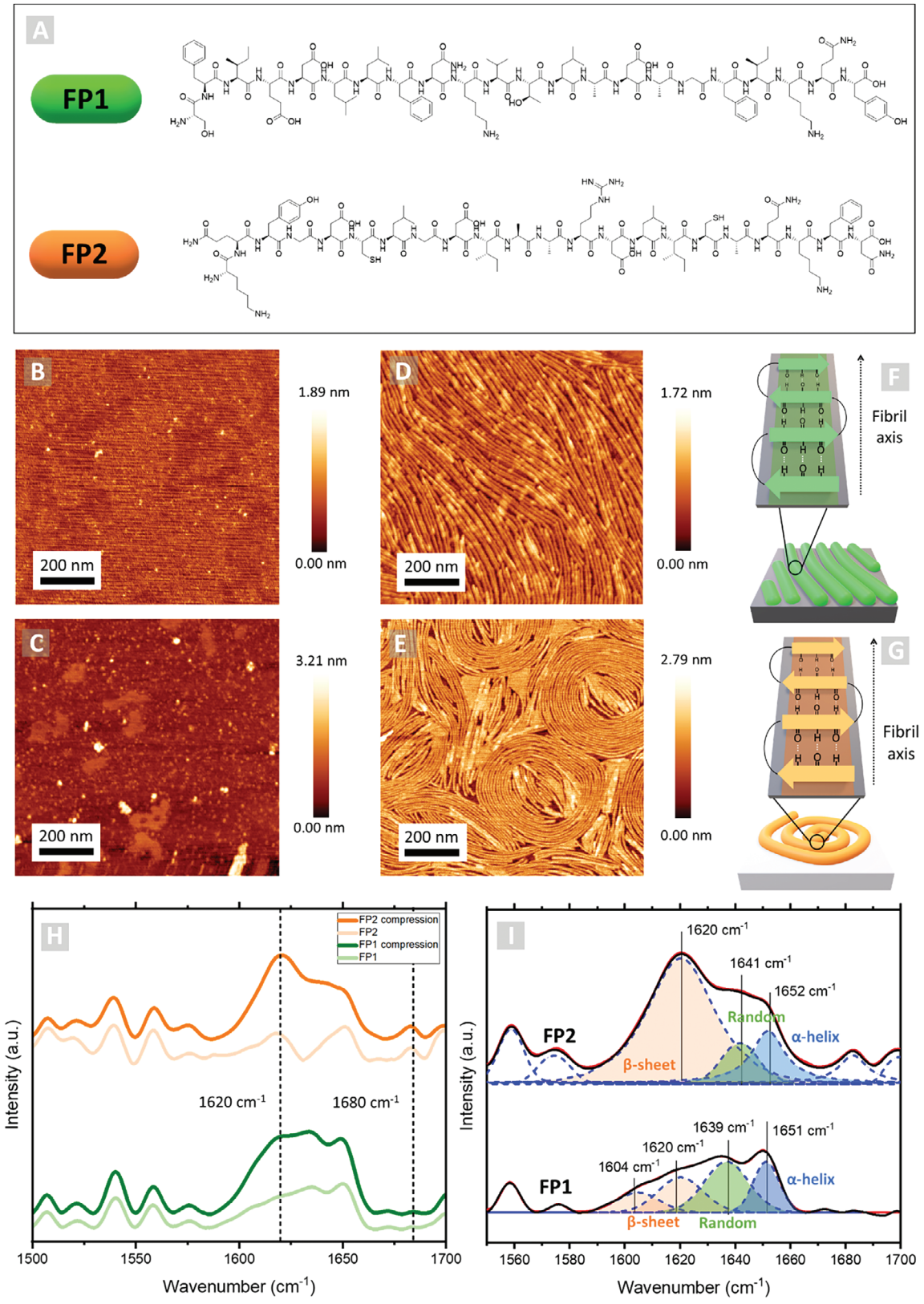

Figure 2. A) Chemical structure of FP1 and FP2 peptides. AFM micrographs of FP1(B, and D) and FP2 (C, and E) peptide LB films transferred onto freshly cleaved mica substrates at no compression (B, and C) and 20 mN m^{-1} (D, and E) respectively. F,G) Schematic representation of the peptides β-sheet secondary structure leading to the formation of the fibers. H) LDIR spectra of the samples studied during this work. I) Deconvolution of the amide I band into their main components.

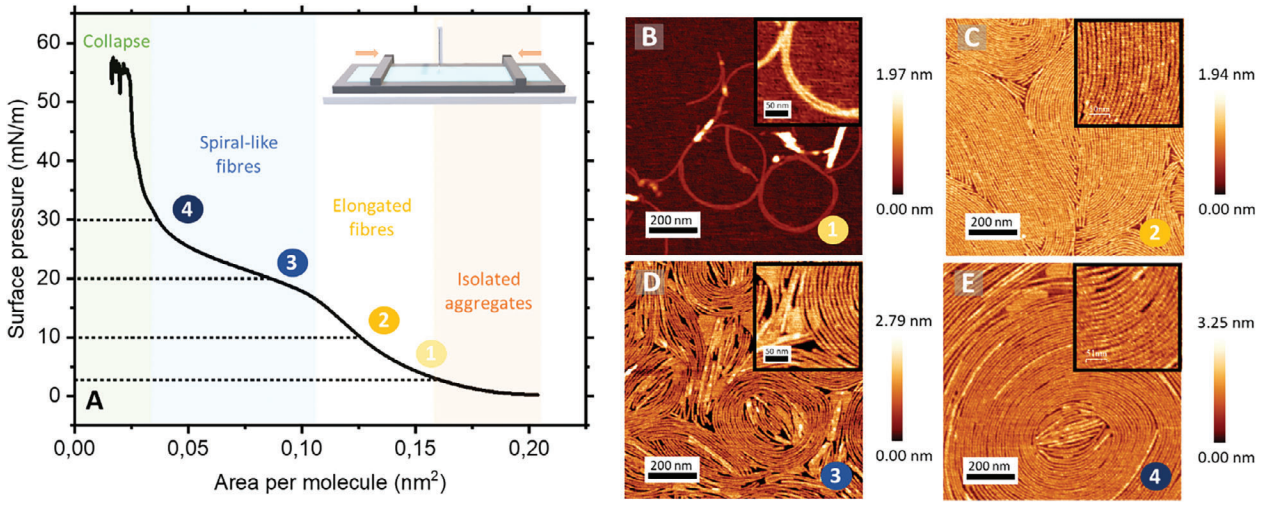

Figure 3. A) $\prod$ – A compression isotherm for the FP2 peptides spread at the air/water interface and AFM micrographs of the LB peptide films obtained at 3, 10, 20, and 30 mN m^{-1} (B, C, D, and E respectively).

a lower L_p and thus show increased flexibility and greater curvature.

Both peptides, which are comparable in sequence length, are initially deposited at the air/water interface, allowing them to orient their hydrophobic residues to interact with the air and their hydrophilic residues to penetrate the subphase. This orientation can facilitate specific alignments and contribute to the different behavior observed between FP1 and FP2 under uniaxial compression in the LB trough.[17] Additionally to the LDIR information, these differences can also be elucidated by examining the chemical structure of both peptides (Figure 2A). FP1, characterized by a higher content of hydrophobic residues such as Leu, Ile, and Val, forms straight fibrils with a rigid morphology, while FP2, containing a mixture of charged and polar residues like Lys, Asp, and Gln, which can selectively disrupt the β-sheet structure due to electrostatic repulsion and solvation effects. This effect results in the formation of flexible fibrils that rearrange into spirals. Noteworthy, FP2 contains cysteine residues capable of forming disulfide bridges within the peptide structure, that may enhance fibril stability but also affect flexibility and morphology.

In summary, the observed differences in fibril morphology are due to variations in the peptide–peptide interactions, secondary structure organization, and overall assembly dynamics between FP1 and FP2 at the interface.

2.5. Variation in Uniaxial Compression Affects FP2 Spiral-Like Nanostructure Morphology

The formation of FP2 peptide spirals was investigated in further detail by varying the uniaxial compression exerted in the LB trough. To do so, **Figure 3A** shows the LB $\prod$–A isotherm alongside the AFM micrographs depicting the various morphologies obtained at different packing densities: prior compression, 3, 10, 20, and 30 mN m^{-1}, respectively). Interestingly, fiber formation initiates even at a very low compression ratio ($A_0/A \approx 0.9$, with A_0 being the initial area per molecule), with isolated fibers emerging at 3 mN m^{-1} (Figure 3B), contrasting the early random-chain peptide aggregates observed prior compression ($A_0/A = 1$; $\prod < 1$ mN m^{-1}) (Figure 2C). With a moderate increase of surface pressure to 10 mN m^{-1}, the resultant nanofibrils are highly homogeneous in length and distribution over the mica surface (Figure 3C). Finally, well-defined spirals are formed as the surface pressure increases to 20 and to 30 mN m^{-1}, respectively (Figure 3D,E).

Taking into consideration the evolution of the fibers ensemble observed with respect to the compression ratio, the observed $\prod$-A isotherm (Figure 3A) can be interpreted as follows: From the early stochastic peptide distribution, a decrease in the compression ratio ($A_0/A < 1$) yields initially a semi-dilute (expanded) organization of peptide chains leading to the formation of elongated fibrils due to excluded volume interactions, in analogy to the description of protein films at the air/water interface.[30,31] Here, the increase in $\prod$ results from the decrease of the available area, as the fibrils come into mutual contact. This can confirm the picture that excluded volume interactions can promote the formation of fibrils. The spatial constraints resulting from the confinement of the peptides to the air/water interface, combined with excluded volume interactions, can lead to the formation of a densely packed assembly at areas $A > 0.125$ nm^2 ($\prod > 15$ mN m^{-1}). This promotes the organization of the fibers in a spiral arrangement and results in a close-packing structure at $A = 0.03$ nm^2 ($\prod \approx 30$ mN m^{-1}) exhibiting solid-like behavior. Further compression ($A_0/A > 6.5$) yields the interfacial jamming of the fibrillar network and the collapse of the film at $\prod =$ 55 mN m^{-1}.

2.6. FP2 Nanofibril Real-Time Assembly at the Air/Water Interface Followed by Neutron Reflectometry

Evaluation of the correlation between the fibril structure in the direction perpendicular to the plane of the air/water interface and the mechanical resistance against shear deformation was done by simultaneous NR and shear rheology experiments. The

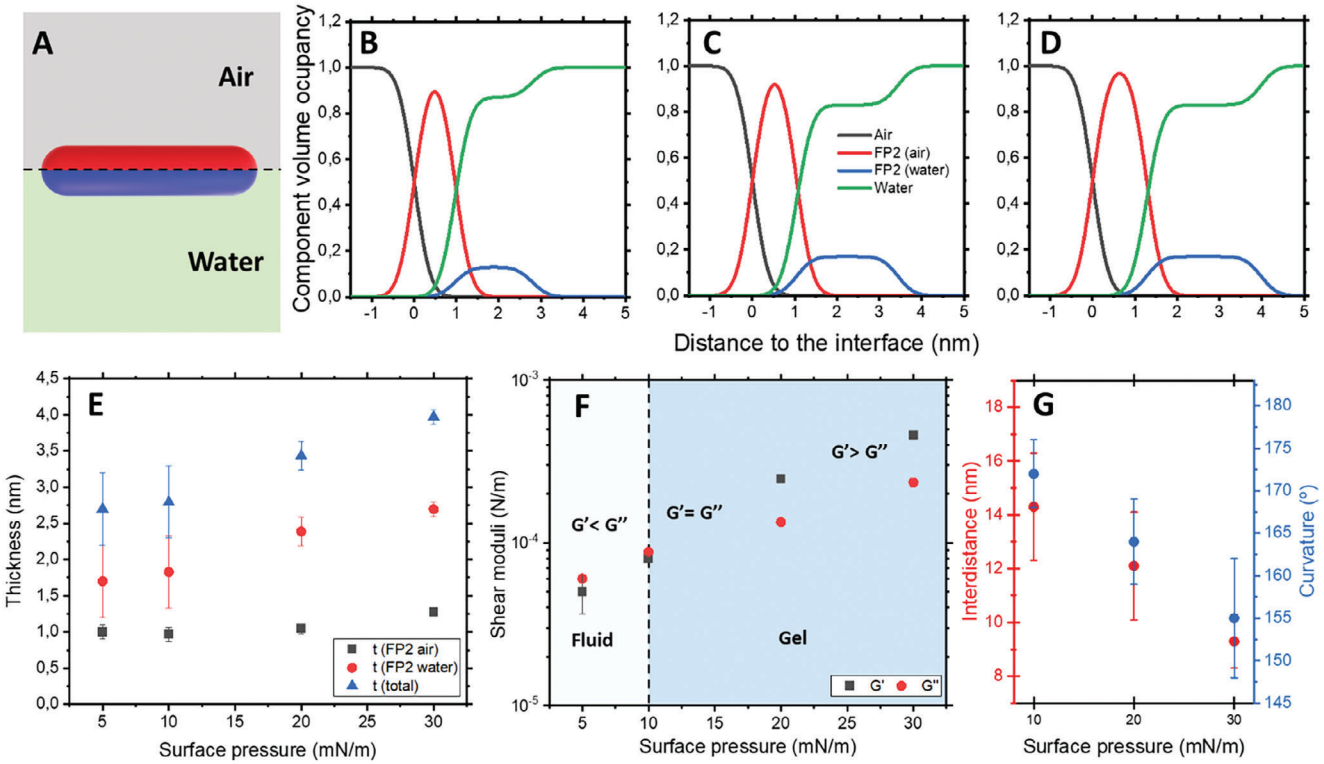

Figure 4. A) Schematic of the model used to fit NR data. Density profiles of the interfaces at B) 10, C) 20, and D) 30 mN m^{-1}. E) The total thickness of the fibers obtained by NR. F) Interfacial shear rheological measurements. G) Interdistance and curvature of the fibers were obtained by analysis of the AFM images.

fibrillar networks assembled at the air/water interface were laterally homogeneous over a length scale comparable to the in-plane neutron coherence length, which is on the order of several microns.[32] The measured R(Q) profiles can therefore be correlated with the averaged scattering length density depth profile across the air/water interface defined by this coherence length. Consequently, the in situ structure of the fibrils as a function of the distance from the interface (z) can be determined. This is done by fitting the reflectivity curves with a parametrized model (See Supporting Information for further details). A model consisting of two layers—one facing the air and the other in contact with the bulk phase outlined in **Figure** 4A—proved to be the most suitable for describing the density profiles of the fibrils perpendicular to the plane of the interface (Figure 4B–D; Figure S6, Supporting Information). The reasoning behind this model is that the fibril network is expected to protrude into the air with a fiber-rich layer close to the interface ($z = 0$) characterized by a finite thickness (t_{air}) and also extend into the aqueous phase (t_{water}). The total thickness of the fibrils normal to the interface ($t = t_{air} + t_{water}$) increases in the vertical direction as surface pressure rises (Figure 4E). This increase is due not only to the protrusion of the fibrils into the air but primarily to their extension into the bulk phase. Remarkably, this thickness evolution observed of the fibrils at the air/water interface can be correlated to those observed in the deposited films onto mica after transferring from the LB trough (Figure 3C–E).

2.7. Interfacial Shear Rheometry Analysis of FP2 Spiral-Like Nanostructure's Resilience

In order to complement in situ NR measurements, the evolution of the FP2 spiral-like nanostructures at different surface pressures was monitored by interfacial shear rheological measurements. The resultant fibril network's shear storage G′ and loss modulus G″ was directly linked to surface pressure (Figure 4F). Below $\prod < 10$ mN m^{-1}, the fibers distributed at the air/water interface can be considered that are in a fluid state, denoted by $G'' > G'$. At $\prod = 10$ mN m^{-1}, $G'' \approx G'$, indicating a clear transition toward a solid regime. Further compression, values of $G'' < G'$ indicates a predominant elastic response that is characteristic of a solid-like regime. This may be explained by the increased number density of fibrils occupying the air/water interface. The higher shear modulus implies a drastic reduction in fibril mobility at the interface. The tightly packed fibril structure generates strong intermolecular forces and resistance to shear deformation. The structural resistance to shear deformation emerging above a critical threshold at $\prod = 10$ mN m^{-1} can therefore be understood as a 2D gel network, where the elastic behavior is due solely to the entropic configurational contribution of the fibrils. We hypothesized that this gel network approach can be therefore based on a statistical physics framework of connected fibrils, where network formation is solely influenced by the molecular packing of fibers at the air/water interface.

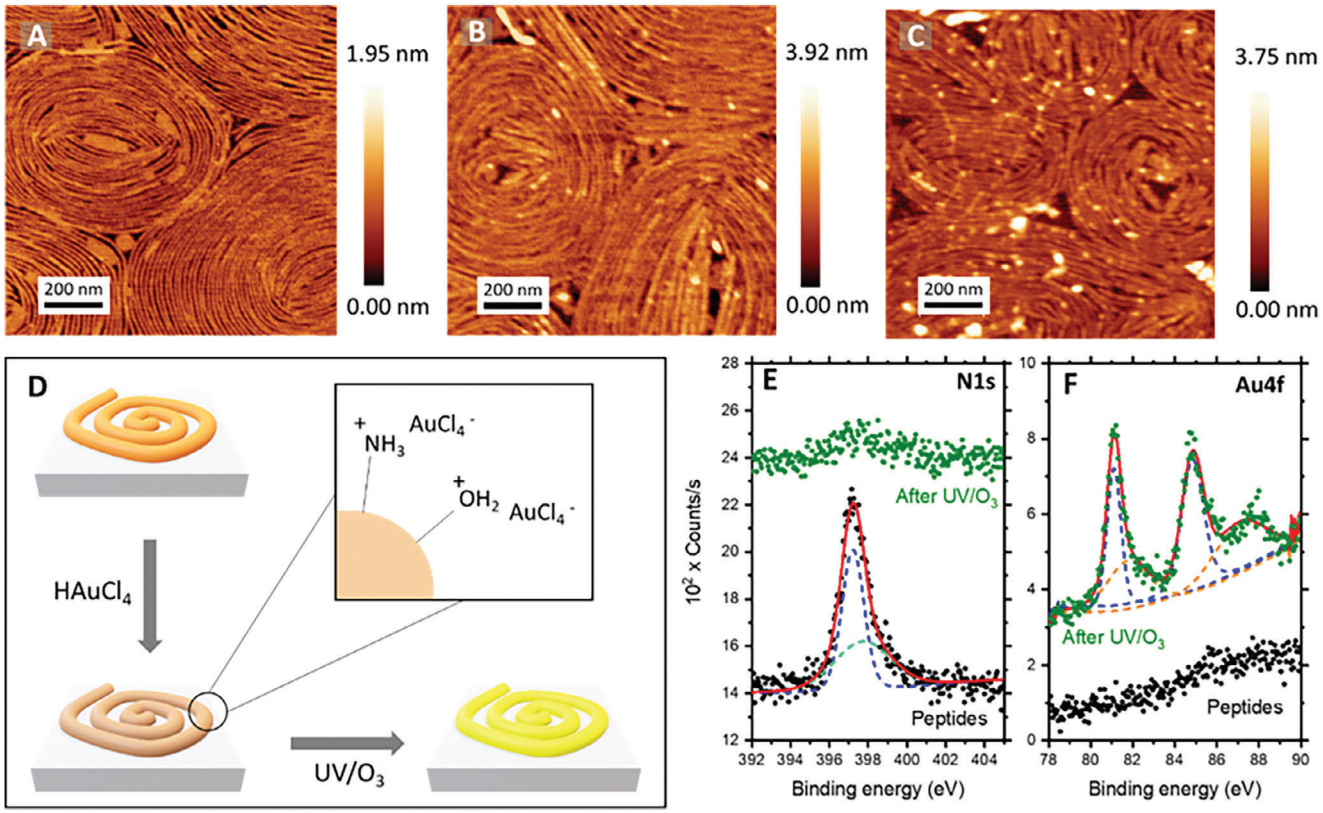

Figure 5. AFM micrographs of the A) pristine FP2 peptides at 20 mN m^{-1} surface pressure onto mica substrates, B) after 30 min immersion into the $HAuCl_4$ solution, and C) after the subsequent UV/O3 degradation treatment. D) Schematic showing the interaction between the peptide fibers and the Au precursor salts in aqueous solutions. High-resolution XPS of E) N 1s and F) Au 4f of pristine FP2 peptides (black dots) and after the inorganic incorporation and UV/O_3 degradation (green dots).

2.8. Controlling FP2 Spiral-Like Morphology Through Uniaxial Compression

The height and width distribution of nanofibrils forming a fluid/solid network appear to be tuneable by controlling the compression ratio in the LB (Figure S7, Supporting Information). The curvature also seems to be remarkably dependent on the uniaxial compression forces applied. In order to quantify this observation θ, across a range of pressures from 10 to 30 mN m^{-1} has been investigated. Figure S8 (Supporting Information) presents the results obtained for this selected set of pressures. The increase in fiber curvature is evident, with θ ranging from 172 ± 4° for fibers compressed at 10 mN m^{-1}, to 164 ± 5° at 20 mN m^{-1}, and 155 ± 7° for the spirals corresponding to 30 mN m^{-1} (Figure 4G).

Another important aspect to consider related to fiber formation under compression and their subsequent bending into spirals is the potential to control the inter-fiber distances with varying compression pressure. In this regard, analysis of the corresponding AFM topographical profiles (Figure 4G), indicates a certain tendency toward contraction of the fiber-to-fiber distance ($D_{f\text{-}f}$) with increasing compression forces, especially for 30 mN m^{-1}. Thus, $D_{f\text{-}f}$ from 10 to 20 mN m^{-1} remains more or less stable around 13 nm (14.3 ± 2 nm vs 12.1 ± 2 nm 10 and 20 mN m^{-1} respectively), decreasing to 9.3 ± 1 nm for 30 mN m^{-1}.

2.9. Inorganic Nanotemplating of FP2 Spiral-Like Nanostructures

Peptide-based nanostructures were previously used as templates for the fabrication of inorganic replicas, by treatment with $HAuCl_4$. This procedure is based on the aqueous metal reduction (AMR) methodology.[33–35] AMR exploits the ionic interactions between the polymer, nucleic acid, or in this case peptide, and the gold ions present in the aqueous solution (**Figure 5D**).

Figure 5A–C shows the AFM micrographs obtained at each step of the fabrication process. Thus, in Figure 5A, the pristine peptide fibers are shown followed by Figure 5B, which depicts the fibers after a 30 min immersion in the metallic precursor aqueous solution, and finally, Figure 5C shows the inorganic replicas obtained after a 20 min UV/O3 treatment. This process serves dual purposes: first, UV has been previously demonstrated as an effective reducing agent for AuIII ions;[36] second, it facilitates the rapid degradation of the peptides, revealing the pure inorganic final structure.[33]

In order to confirm the effectiveness of the etching process via UV/O_3 and the successful incorporation of inorganic species, samples were characterized by X-ray photoelectron spectroscopy (XPS). The etching process can be followed by the N 1s XPS spectrum as nitrogen groups are characteristic markers of the peptide structure. Thus XPS spectra presented in Figure 5E demonstrate that after 20 min of UV/O3 treatment, complete degradation of

the peptide fibers occurs. On the other hand, the Au 4f XPS spectrum presented in Figure 5F, confirms the successful impregnation of the peptide fibers with the Au precursors. However, even if 20 min of UV/O_3, seems enough for the degradation of the peptide structure, it appears insufficient for achieving full reduction of the gold replicas obtained. Consequently, some residual Au^I (87.8 and 82.9 eV – orange dotted line in Figure 5F), is still detected after the UV/O_3 treatment, while the majority of the Au^{III} precursor has been reduced to Au^0 (84.2 and 81.0 – blue dotted line in Figure 5F). The formation of the inorganic structures was further confirmed by analyzing the surface adhesion force measurements obtained by AFM. The peptide-based structures exhibit low adhesion forces, as shown in Figure S9A (Supporting Information), which can be attributed to their highly hydrophobic nature. The removal of the peptides is confirmed by an increase in adhesion force, which is also due to the increased exposure of the silicon substrate, known for its high adhesion force relative to the silicon-based AFM tip. Additionally, the presence of gold fibers is confirmed by their lower affinity to the AFM tip, along with some gold aggregates formed during the templating process (Figure S9B, Supporting Information).

The inorganic templating methodology developed here can be applied to different inorganic species, as depicted in Figure S10 (Supporting Information). This demonstrates the versatility and reliability of this fabrication approach in producing highly uniform sub-10 nm metallic features. Such precision is challenging to achieve with existing lithographic techniques like block copolymers[37,38] or e-beam lithography,[39] showing the great potential of peptide-guide self-assembly as an additional technique for surface templating at the nanoscale over large surface areas at a low energy input.

3. Conclusion

We have demonstrated the remarkable ability of viral fusion peptide sequences to form resilient spiral-like structures from nanofibrils within a Langmuir trough. Moreover, by controlling the compression forces at the air–water interface, nanofibrils with specific curvature and inter-fiber distances have been obtained. A fluid-to-solid transition has been also evidenced by uniaxial compression, resulting in the formation of a gel network, as demonstrated by shear rheology. The fabrication methodology presented here introduces uniaxial-contraction methodologies as a robust and effective approach for fabricating highly homogeneous monolayers of peptide fibers and transferring these onto solid substrates. Finally, spiral-like structures serve as templates for fabricating gold metallic replicas. This multi-technique approach not only deepens our comprehension of peptide self-assembly but also reveals novel scenarios for engineering functional nanomaterials.

4. Experimental Section

Materials: FP1 (SARS-CoV-2 816-SFIEDLLFNKVTLADAGFIKQY-837) and FP2 (SARS-CoV-2 835-KQYGDCLGDIAARDLICAQKFN-856) fusion peptides were synthesized and purified by GenScript (Amsterdam, The Netherlands). 0.5 mg mL^{-1} stock solutions of each peptide in DMSO (dimethyl sulfoxide, anhydrous, ≥99.9%, Merck) were used for all the experiments reported here. Tetrachloroauric(III) acid trihydrate (HAuCl4) 99% was purchased from Sigma Aldrich and used as received. Mica surfaces (discs with 12 mm of diameter and 0.15 mm thickness) were purchased via Electron Microscopy Science. Au-coated Si substrates (100 nm, Sigma–Aldrich, 10 × 10 mm^2) served for FTIR measurements.

Langmuir Trough Experiments and Langmuir-Blodgett (LB) Deposition: The surface pressure ($\prod$) – area (A) isotherms were acquired using a Langmuir trough (model G2, KIBRON, Helsinki, Finland). FP1 and FP2 peptides were dispersed in DMSO at a concentration of 0.5 mg mL^{-1}. Subsequently, the LB trough was filled with de-ionized water (Milli-Q, Millipore; resistivity higher than 18 MW; organic matter lower than 1 ppb). Next, a Hamilton micrometre syringe was employed to spread the corresponding peptide solution in DMSO (150 µL) onto the subphase (250 mL). Following DMSO evaporation, surface pressure variation during mechanical, uniaxial compression imposed by the barriers of the Langmuir trough (at a compression speed of 8 cm^2 min^{-1}) was monitored using a Wilhelmy plate paper (Whatman CHR1 chromatography paper) connected to an electrobalance. The subphase temperature was maintained throughout the experiments at 21.0 ± 0.5 °C. Upon reaching the desired surface pressure (3, 10, 20, and 30 mN m^{-1} respectively), LB peptide films were transferred onto mica substrates (withdrawn speed was set up at 0.5 mm min^{-1}).

Neutron Reflectometry (NR) and Interfacial Shear Rheology (ISR) Experiments: Simultaneous NR and ISR measurements were conducted on the time-of-flight reflectometer FIGARO at the ILL. For NR, two different angles of incidence ($\theta = 0.6°$ and 3.7°) and a wavelength resolution of 7% $d\lambda/\lambda$, were used yielding a momentum transfer, $Q = (4\pi/\lambda)\sin\theta$, range from 0.007 to 0.25 $Å^{-1}$. The reflected neutron beam was detected by a 2D ^3He detector and the raw time-of-flight experimental data at these two angles of incidence were calibrated to the incident wavelength distribution and the efficiency of the detector. The resulting reflectivity profiles R, defined as the ratio of the intensity of the neutrons scattered at the air–water interface over the incident intensity of the neutron beam, were reported against Q.

NR experiments were performed in a Langmuir trough using a subphase composed of 8.1% D_2O (v/v) known as air contrast matched water (ACMW) since its scattering length density is equal to the one of air. Subsequent data analysis was performed using Motofit software (see Supporting Information, SI). Optimization of model parameters was done by the combined use of a genetic algorithm for efficient search of the parameter space, and a Levenberg-Marquadt non-linear least-square algorithm for a final refinement of the fitting parameters. The quality of the fits was reported as reduced χ^2.

The mechanical response of the monolayers under shear deformation was measured using an interfacial shear rheometer (ISR) in combination with the FIGARO reflectometer at ILL to simultaneously acquire rheological and structural data. The ISR is composed of an Anton Paar MCR 702e Space rotational rheometer complemented with a homemade Double Wall-Ring (DWR) geometry.[40] Full details on the experimental setup will be reported elsewhere.[41] Small amplitude oscillatory measurements at a frequency of 0.5 Hz were carried out controlling the applied shear strain on the monolayer at 3%. No strong shear thinning effects have been observed below strain values of 4%. The analysis of the rheological data is made using a purposely designed computer code based on the calculation of the hydrodynamic velocity fields at the interface and at the surrounding bulk fluid phases.[42]

Nanotemplating: Solutions (0.1 wt.%) of HAuCl4 in milli-Q water were used to impregnate the peptide fibers by immersion of the sample in the solution for 30 min. Subsequently, hybrid samples were exposed to a UV/O_3 cleaner (Ossila, UK) for 20 min in order to remove the peptide template and reduce the gold salts.

Atomic Force Microscopy (AFM): All images were obtained with a multimode AFM and a Nanoscope V controller (Bruker). The AFM was operated in PeakForce Quantitative Nanomechanics (QNM) mode in air, at room temperature. A silicon tip (PNP-DB, NanoAndMore GmbH, Germany), with a spring constant of 0.48 N/m and a resonant frequency of 300 kHz, was used for scanning. Images were taken at a scan rate of 1 Hz and 512 × 512 pixels, using the Nanoscope Software. All AFM images were analyzed using the WSxM software.[43]

Laser-Directed Infrared Spectroscopy (LDIR): LDIR spectra were measured on Au-coated silicon substrates functionalized with the peptide fibers (fabricated using a similar methodology to mica surfaces) using an IR Imaging systems IR Agilent LDIR 8700. To minimize potential interference from water band absorption around 1630–1650 cm^{-1}, samples were stored under vacuum for 48 h prior to LDIR measurements.

Supporting Information

Supporting Information is available from the Wiley Online Library or from the author.

Acknowledgements

A.A-.F. and N.P. contribute equally to this work. The authors thank the Institut Laue-Langevin (https://doi.ill.fr/10.5291/ILL-DATA.9-11-2199)) for the allocation of beamtime and the Partnership for Soft Condensed Matter (PSCM) for the lab support. A.M. acknowledges the financial support from MICINN under grant PID2021-129054NA-I00, and from the Department of Education of the Basque Government under grant PIBA_2023_1_0054 and from the IKUR Strategy under the collaboration agreement between Ikerbasque Foundation and Materials Physics Center. AAF is grateful for support from the Provincial Council of Gipuzkoa under the program Fellow Gipuzkoa. The authors thank the technical and human support provided by SGIker (UPV/EHU/ERDF, EU) in conducting the LDIR and XPS measurements.

Conflict of Interest

The authors declare no conflict of interest.

Data Availability Statement

The data that support the findings of this study are available from the corresponding author upon reasonable request.

Keywords

fibers, inorganic templating, nanostructuration, neutron reflectometry, peptide self-assembly

Received: June 24, 2024
Revised: October 21, 2024
Published online:

[1] R. B. Davidson, J. I. Ziegler, G. Vargas, S. M. Avanesyan, Y. Gong, W. Hess, R. F. Haglund, *Nanophotonics* **2015**, *4*, 108.
[2] S. A. Asefa, S. Shim, M. Seong, D. Lee, *Appl. Sci.* **2023**, *13*, 10590.
[3] B. Yu, Q. Yang, H. Li, Z. Liu, X. Huang, Y. Wang, H. Chen, *J. Colloid Interface Sci.* **2019**, *533*, 304.
[4] R. McGorty, J. Fung, D. Kaz, V. N. Manoharan, *Mater. Today* **2010**, *13*, 34.
[5] A. Maestro, *Curr. Opin. Colloid Interface Sci.* **2019**, *39*, 232.
[6] F. Grillo, M. A. Fernandez-Rodriguez, M.-N. Antonopoulou, D. Gerber, L. Isa, *Nature* **2020**, *582*, 219.
[7] X. Huang, C. Li, S. Jiang, X. Wang, B. Zhang, M. Liu, *J. Colloid Interface Sci.* **2005**, *285*, 680.
[8] X. Huang, C. Li, S. Jiang, X. Wang, B. Zhang, M. Liu, *J. Am. Chem. Soc.* **2004**, *126*, 1322.
[9] Y. Zhang, P. Chen, L. Jlang, W. Hu, M. Llu, *J. Am. Chem. Soc.* **2009**, *131*, 2756.
[10] D. Mandal, A. Nasrolahi Shirazi, K. Parang, *Org. Biomol. Chem.* **2014**, *12*, 3544.
[11] A. Levin, T. A. Hakala, L. Schnaider, G. J. L. Bernardes, E. Gazit, T. P. J. Knowles, *Nat. Rev. Chem.* **2020**, *4*, 615.
[12] I. W. Hamley, *Soft Matter* **2011**, *7*, 4122.
[13] L. Wang, G. Shen, X. Yan, *Particuology* **2022**, *64*, 14.
[14] J. Wang, K. Liu, R. Xing, X. Yan, *Chem. Soc. Rev.* **2016**, *45*, 5589.
[15] H. Wen, J. Yao, X. Chen, S. Ling, Z. Shao, *Nano Res.* **2023**, *16*, 1414.
[16] A. Santamaria, K. C. Batchu, O. Matsarskaia, S. F. Prévost, D. Russo, F. Natali, T. Seydel, I. Hoffmann, V. Laux, M. Haertlein, T. A. Darwish, R. A. Russell, G. Corucci, G. Fragneto, A. Maestro, N. R. Zaccai, *J. Am. Chem. Soc.* **2022**, *144*, 2968.
[17] G. Forte, A. Grassi, G. Marletta, *J. Phys. Chem. B* **2007**, *111*, 11237.
[18] F. Zhang, H. Du, Z. Zhang, L. Ji, H. Li, L. Tang, H. Wang, C. Fan, H. Xu, Y. Zhang, J. Hu, H. Hu, J. He, *Angew. Chem., Int. Ed.* **2006**, *45*, 3611.
[19] S. Jun, Y. Hong, H. Imamura, B. Y. Ha, J. Bechhoefer, P. Chen, *Biophys. J.* **2004**, *87*, 1249.
[20] M. A. Strehle, P. Rösch, R. Petry, A. Hauck, R. Thull, W. Kiefer, J. Popp, *Phys. Chem. Chem. Phys.* **2004**, *6*, 5232.
[21] A. Barth, C. Zscherp, *Q. Rev. Biophys.* **2002**, *35*, 369.
[22] A. Drozdetskiy, C. Cole, J. Procter, G. J. Barton, *Nucleic Acids Res.* **2015**, *43*, W389.
[23] H. A. Lashuel, S. R. LaBrenz, L. Woo, L. C. Serpell, J. W. Kelly, *J. Am. Chem. Soc.* **2000**, *122*, 5262.
[24] M. Sunde, L. C. Serpell, M. Bartlam, P. E. Fraser, M. B. Pepys, C. C. F. Blake, *J. Mol. Biol.* **1997**, *273*, 729.
[25] P. C. Ke, R. Zhou, L. C. Serpell, R. Riek, T. P. J. Knowles, H. A. Lashuel, E. Gazit, I. W. Hamley, T. P. Davis, M. Fändrich, D. E. Otzen, M. R. Chapman, C. M. Dobson, D. S. Eisenberg, R. Mezzenga, *Chem. Soc. Rev.* **2020**, *49*, 5473.
[26] S. E. Taylor, B. Desbat, D. Blaudez, S. Jacobi, L. F. Chi, H. Fuchs, G. Schwarz, *Biophys. Chem.* **2000**, *87*, 63.
[27] O. Kratky, G. Porod, *J. Colloid Sci.* **1949**, *4*, 35.
[28] C. Rivetti, M. Guthold, C. Bustamante, *J. Mol. Biol.* **1996**, *264*, 919.
[29] C. C. vandenAkker, M. F. M. Engel, K. P. Velikov, M. Bonn, G. H. Koenderink, *J. Am. Chem. Soc.* **2011**, *133*, 18030.
[30] R. Mezzenga, P. Fischer, *Rep. Prog. Phys.* **2013**, *76*, 046601.
[31] P. Cicuta, E. M. Terentjev, *Eur. Phys. J. E* **2005**, *16*, 147.
[32] A. Maestro, P. Gutfreund, *Adv. Colloid Interface Sci.* **2021**, *293*, 102434.
[33] A. Alvarez-Fernandez, K. Aissou, G. Pécastaings, G. Hadziioannou, G. Fleury, V. Ponsinet, *Nanoscale Adv.* **2019**, *1*, 849.
[34] C. Cummins, T. Ghoshal, J. D. Holmes, M. A. Morris, *Adv. Mater.* **2016**, *28*, 5586.
[35] E. A. Karpushkin, Y. D. Aleksandrov, A. V. Gibalova, A. M. Abakumov, L. I. Lopatina, V. G. Sergeyev, *Colloid. Polym. Sci.* **2019**, *297*, 433.
[36] J. J. Zou, Y. P. Zhang, C. J. Liu, *Langmuir* **2006**, *22*, 11388.
[37] C.-C. Liu, *Nat. Electron* **2018**, *1*, 562.
[38] R. M. Jacobberger, V. Thapar, G. P. Wu, T. H. Chang, V. Saraswat, A. J. Way, K. R. Jinkins, Z. Ma, P. F. Nealey, S. M. Hur, S. Xiong, M. S. Arnold, *Nat. Commun.* **2020**, *11*, 4151.
[39] Y. Chen, Z. Shu, S. Zhang, P. Zeng, H. Liang, M. Zheng, H. Duan, *Int. J. Extr. Manufact.* **2021**, *3*, 032002.

[40] S. Vandebril, A. Franck, G. G. Fuller, P. Moldenaers, J. Vermant, S. Vandebril, P. Moldenaers, J. Vermant, A. Franck, G. G. Fuller, *Rheol. Acta* **2010**, *49*, 131.
[41] P. Sanchez-Puga, J. Carrascosa, J. Tajuelo, A. Maestro, P. Gutfreund, M. A. Rubio, arXiv:2411.04660.
[42] P. Sánchez-Puga, J. Tajuelo, J. M. Pastor, M. A. Rubio, *Adv. Colloid Interface Sci.* **2021**, *288*, 102332.
[43] J. M. Gómez-Rodríguez, I. Horcas, J. Gómez-Herrero, A. M. Baro, J. Colchero, R. Fernández, *Rev. Sci. Instrum.* **2007**, *78*, 013705.